nature physics

ARTICLES

PUBLISHED ONLINE: 1 AUGUST 2016 | DOI: 10.1038/NPHYS3838

Supercurrent in a room-temperature Bose–Einstein magnon condensate

Dmytro A. Bozhko[1,2], Alexander A. Serga[1], Peter Clausen[1], Vitaliy I. Vasyuchka[1], Frank Heussner[1], Gennadii A. Melkov[3], Anna Pomyalov[4], Victor S. L'vov[4] and Burkard Hillebrands[1]*

A supercurrent is a macroscopic effect of a phase-induced collective motion of a quantum condensate. So far, experimentally observed supercurrent phenomena such as superconductivity and superfluidity have been restricted to cryogenic temperatures. Here, we report on the discovery of a supercurrent in a Bose–Einstein magnon condensate prepared in a room-temperature ferrimagnetic film. The magnon condensate is formed in a parametrically pumped magnon gas and is subject to a thermal gradient created by local laser heating of the film. The appearance of the supercurrent, which is driven by a thermally induced phase shift in the condensate wavefunction, is evidenced by analysis of the temporal evolution of the magnon density measured by means of Brillouin light scattering spectroscopy. Our findings offer opportunities for the investigation of room-temperature macroscopic quantum phenomena and their potential applications at ambient conditions.

The term supercurrent is commonly assigned to a resistance-free charge current in a superconductor or to a viscosity-free particle current in superfluid ^{4}He or ^{3}He. More generally, this macroscopic quantum phenomenon relates to the collective motion of bosons (including real atoms[1,2], Cooper pairs of fermions[3,4] and bosonic quasiparticles[5–10]) coalescing into the same quantum state and, thus, constituting a specific state of matter described by a single, coherent wavefunction, a Bose–Einstein condensate (BEC)[11–14]. It is remarkable that any type of supercurrent is induced not by an external driving force but by a phase gradient in the BEC wavefunction.

Up to now this prominent effect has been observed only at rather low temperatures. For example, spin supercurrents[5,15] and such related phenomena as the spin Josephson effect[16] and spin quantum vortices[17] have been discovered in a system of nuclear spins in liquid ^{3}He (ref. 18). At the same time, it is known that a BEC can be prepared even at room temperature by a strong increase in the density[19] of weakly interacting quasiparticles such as photons[20], plasmon-exciton polaritons[21] or magnons[22,23]. In addition, recent theoretical studies predict the existence of Josephson and phase-driven persistent BEC currents in a parametrically pumped magnon gas[24–26].

Here, we present experimental evidence for the excitation of a supercurrent in a magnon BEC at room temperature in a ferrimagnetic insulator. The temporal evolution of the magnon BEC formed in a parametrically populated magnon gas was studied by Brillouin light scattering spectroscopy (BLS)[27,28]. It has been found that heating in the focus of a probing laser beam locally enhances the decay of the magnon condensate, but does not alter the relaxation dynamics of gaseous magnons. Our understanding of this effect is based on the temperature-induced spatial variation in the saturation magnetization and, thus, on the variation in the local magnon frequencies across the heated sample area. Because the magnon condensate is coherent across the entire heated area, a spatially varying phase shift is imprinted into its wavefunction. This spatial phase gradient propels a magnon supercurrent that flows to the BEC areas surrounding the focal spot and, thus, decreases the BEC density in the probing point. The detailed quantitative agreement between our experiments and a rate-equation model, which considers the temperature-induced supercurrent jointly with a dispersion-caused magnon counter-current, provides a compelling proof for a supercurrent in a room-temperature Bose–Einstein magnon condensate.

We have studied the appearance of the magnon supercurrent by observing the temporal evolution of a magnon BEC in an in-plane magnetized single-crystal yttrium iron garnet (YIG, $Y_3Fe_5O_{12}$) film (see inset in Fig. 1). YIG is a ferrimagnetic dielectric material with unique low magnon damping[29], allowing both for efficient thermalization of externally injected magnons and for a BEC lifetime of several hundred nanoseconds. To achieve Bose–Einstein condensation[23,30], magnons are injected into the YIG spin system via parallel parametric pumping[31], which currently is considered to be the most efficient technique for magnon excitation over a large wavevector range. The process can be described by a splitting of a photon of a pumping electromagnetic wave with nearly zero wavevector and the pumping frequency ω_p into two magnons with opposite wavevectors $\pm\boldsymbol{q}$ and frequency $\omega_p/2$. This magnon injection process is schematically illustrated by the red arrow in Fig. 1, which shows the dipole-exchange magnon spectrum[32] calculated for the given experimental conditions using a method described in ref. 33.

The strength of the bias magnetic field $H = 1{,}690$ Oe is chosen to allow for magnon injection slightly above the ferromagnetic resonance frequency ω_{FMR}, where the parallel pumping process has its highest efficiency[34,35]. When the injected magnons thermalize through scattering processes conserving both their number and the total energy[36,37], a BEC may be formed at the lowest energy state of the energy–momentum spectrum (see Fig. 1) even at room temperature[23,30]. Notice that, in the chosen magnetization geometry, the strong magnetic dipole–dipole interaction results in

[1]Fachbereich Physik and Landesforschungszentrum OPTIMAS, Technische Universität Kaiserslautern, 67663 Kaiserslautern, Germany. [2]Graduate School Materials Science in Mainz, 67663 Kaiserslautern, Germany. [3]Faculty of Radiophysics, Electronics and Computer Systems, Taras Shevchenko National University of Kyiv, Kyiv 01601, Ukraine. [4]Department of Chemical Physics, Weizmann Institute of Science, Rehovot 76100, Israel.
*e-mail: hilleb@physik.uni-kl.de

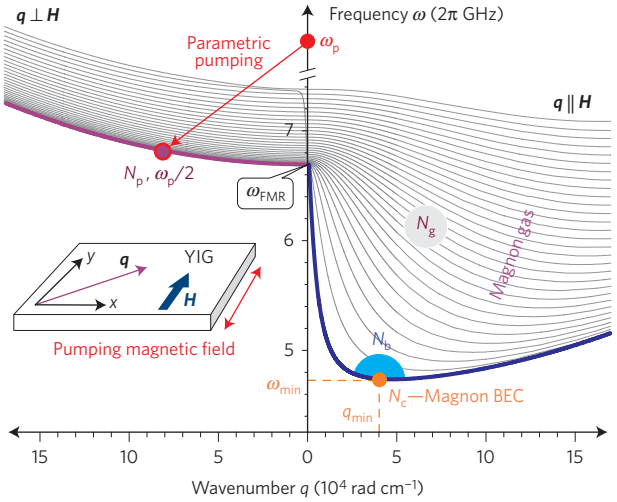

Figure 1 | Magnon spectrum. Magnon spectrum of a 5.6-μm-thick YIG film magnetized in plane by a bias magnetic field $H=1{,}690$ Oe, shown for the wavevector $\boldsymbol{q}$ perpendicular (left) and parallel (right) to the applied field. For both wavevector directions the first 31 thickness modes are shown. The red arrow illustrates the magnon injection process by means of parallel parametric pumping. N_p, total number of parametrically excited magnons at $\omega_p/2$; N_c, number of BEC magnons at $\omega_c=\omega_{min}$; N_b, number of gaseous magnons near ω_{min} and q_{min}; N_g, number of magnons in the parametrically overpopulated gas of magnons below $\omega_p/2$. The inset schematically shows the geometry of the in-plane magnon wavevector $\boldsymbol{q}$, the bias field $\boldsymbol{H}$, and the pumping microwave magnetic field.

two symmetric minima in the frequency spectrum $\omega(\boldsymbol{q})$ at $\boldsymbol{q}=\pm\boldsymbol{q}_{min}$ (with $\boldsymbol{q}_{min} \parallel \boldsymbol{H}$) and, consequently, in the fact that a system of two BECs is created[38]. Similar to other systems with coexisting BEC states (see, for example, ref. 39), the physics of this BEC system is much richer then the physics of the majority of BECs of particles having only one spectral minimum at $q=0$. Currently, the study of the two-valley BEC is still in its infancy stage (see, for example, refs 24,38,40).

The experimental set-up, which consists of a YIG film, a microwave circuit and a wavevector- and time-resolved BLS system (see Methods), is schematically shown in Fig. 2a. The microwave pumping circuit comprises a microwave source, a switch, and an amplifier. This circuit drives a 50-μm-wide microstrip resonator, which is placed below the YIG film. The resonator concentrates the applied microwave energy and induces a microwave Oersted field oriented along the bias magnetic field $\boldsymbol{H}$, thus realizing conditions for the parallel parametric pumping mechanism. The pumping pulses of $\tau_P=2\,\mu s$ duration are applied with a repetition time of 1 ms, allowing for magnetic and temperature equilibration of the YIG film.

In our experiment, a focused laser beam combines the role of the magnon probe in the BLS experiment with the role of the local sample heater. The heating time is adjusted by chopping the probing laser beam using an acousto-optic modulator (AOM). The laser pulse duration τ_L is varied between 6 μs and 80 μs. By changing τ_L, the set-up allows one to change the heating time interval before the application of the microwave pumping pulse and, consequently, to control the sample temperature in the probing point (see Fig. 2b). The modulated probing beam is focused onto the surface of the YIG film in the middle of the microstrip resonator (see Fig. 2a,c), where it has a maximum peak power of 9.5 mW. The focal spot has a radius $R\approx 10\,\mu m$ and, thus, is approximately half the size of the 50-μm-wide parametric pumping area. The scattered light is deflected by the beam splitter to the tandem Fabry–Pérot interferometer, which selects the frequency-shifted components of the scattered light. The intensity of the inelastically scattered light, which is proportional to the magnon density in the probing point, is detected and analysed in time (see Methods).

To understand the dynamics of the magnon BEC, one first needs to separate the effects caused by the spatially uniform change of the sample temperature from those caused by the formation of a temperature gradient. Therefore, in a first experiment, we combined BLS probing at low laser power with an uniform heating of the YIG sample by a hot air flow. Figure 3a shows the typical dynamics of the magnon BEC in this case. During the action of the pump pulse the magnon density increases and saturates. After the parametric pumping is switched off, the magnon density jumps up due to the previously reported intensification of the BEC formation in the freely evolving magnon gas[30]. Afterwards the magnon density exponentially decreases due to the conventional spin–lattice relaxation mechanisms. This behaviour is common for all temperatures in our experiment. Some decrease in the steady-state magnon density observed at higher temperatures can be related both to higher magnon damping[29] and to lower efficiency of the parametric pumping in this case. The latter effect is straightforward:

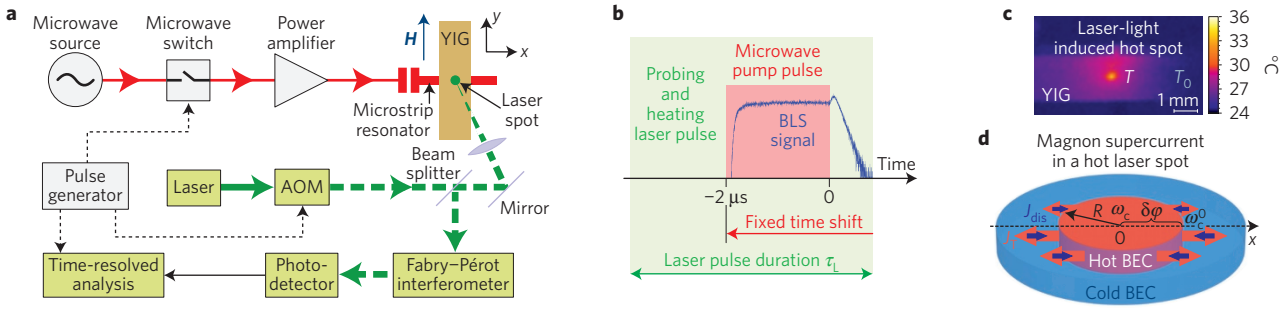

Figure 2 | Experimental set-up. a, Schematic illustration of the experimental set-up. The upper part of the figure shows the microwave circuit, consisting of a microwave source, a switch and an amplifier. This circuit drives a microstrip resonator, which is placed below the in-plane magnetized YIG film. Light from a solid-state laser ($\lambda_L=532$ nm) is chopped by an acousto-optic modulator (AOM) and guided to the YIG film. There it is scattered inelastically from magnons, and the frequency-shifted component of the scattered light is selected by the tandem Fabry–Pérot interferometer, detected, and analysed in time. **b**, Time diagram presenting the relative timing of the microwave pump pulse, the laser pulse, and the detected BLS signal. **c**, Infrared photo of the YIG sample, showing the hot spot in the focus of the probing laser beam. **d**, Schematic illustration of a supercurrent flowing in the magnon BEC subject to a thermal gradient. Red arrows—outflow of the thermally induced supercurrent J_T from the hot focal spot. Blue arrows—contraflow of the dispersive current J_{dis}. ω_c and ω_c^0, magnon BEC phases in the hot and in the cold parts of the sample, respectively. $\delta\varphi$, temperature induced phase accumulation in the magnon BEC; R, radius of the hot spot.

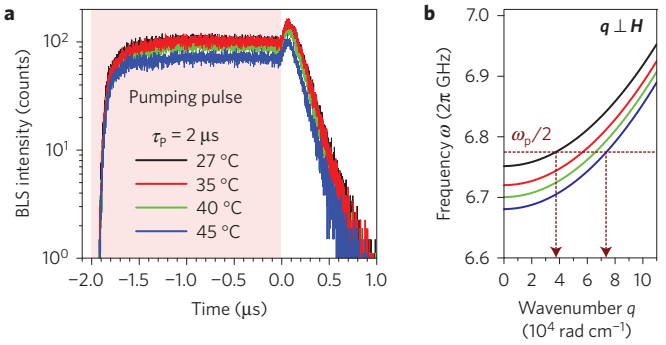

Figure 3 | Temperature-dependent temporal dynamics of the magnon BEC. a, Time-resolved BLS intensity for different uniform temperatures of the YIG film. The sample temperature was measured by an infrared camera. Magnons were detected near their spectral energy minimum in a frequency band of 100 MHz spectral width. **b**, Influence of the YIG film temperature on the spin-wave dispersion (same colour code for temperature as in **a**).

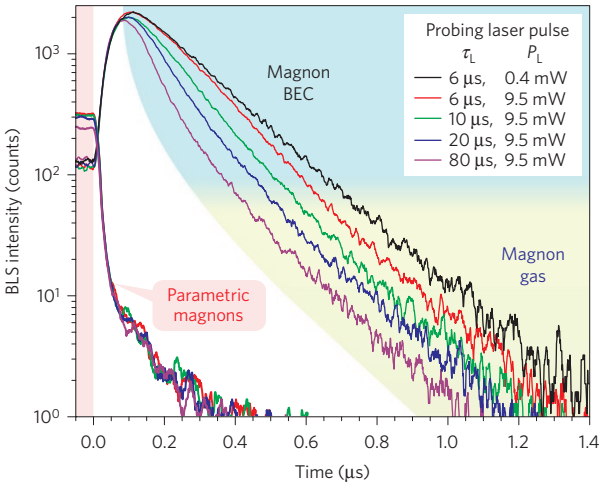

Figure 4 | Temporal dynamics of the magnon BEC under local laser heating. The increase of the laser pulse duration, and thus the heating time, leads to a faster decay of the magnon BEC in the measurement spot—that is, the laser spot. The relaxation dynamics of the residual gaseous magnons, which starts to be visible after the disappearance of the BEC, is independent of the heating. Blue and yellow shadings mark the areas of coherent (BEC) and non-coherent (gaseous phase) magnon dynamics, respectively. The magnons parametrically injected at $\omega_p/2$ show no temperature-related change in their nonlinear relaxation dynamics after the end of the pumping pulse.

due to a lowered saturation magnetization at higher temperatures the parametrically populated spectral magnon branch shifts towards lower frequencies (see Fig. 3b). At constant parametric pumping frequency this shift increases the wavenumber of the injected magnons and, consequently, the threshold power of the parametric generation[34].

Now we focus on the temperature-gradient-dependent behaviour of the magnon condensate. Figure 4 shows the evolution of the magnon density at the bottom of the spin-wave spectrum for four different heating times—that is, for four values of the temperature gradient—at a laser power of $P_L = 9.5$ mW. For comparison, the black curve presents the time-dependent magnon dynamics measured using a much lower laser power of 0.4 mW. Similar to Fig. 3a, the BLS signal rises sharply after the microwave pumping pulse is switched off due to the intensification of the BEC formation process[30]. Afterwards, the magnon density decreases. In the case of low-power laser probing this decrease has an exponential form with a characteristic decay time $\tau \simeq 240$ ns, which corresponds well to the conventional values of a linear magnetic decay in YIG films[29] in the vicinity of ω_{min}—that is, for both the magnon BEC and the gaseous magnons near the bottom of the spectrum.

At higher laser power the observed decrease in the magnon density can no longer be described by a single exponential function. Two different regimes of the magnon decay are clearly visible from the slopes of the BLS signals presented in Fig. 4. In the first regime, at high BLS intensities (the blue shaded area in Fig. 4), the decay of the magnon density depends on the heating duration—that is, on the temperature gradient in the laser focal spot. In the second regime, at low BLS intensities (the yellow shaded area in Fig. 4), this decay is independent of temperature and its rate coincides with that observed in the low-laser-power experiment. It is remarkable that, for all heating durations, the transition between these two decay regimes occurs at approximately the same magnon density level, which can be associated with the transition from the condensed to the gaseous magnon phase.

It is also worth analysing the evolution of parametrically injected magnons (see Fig. 4), which play the important role of a magnon source for all other spectral states of the magnon gas and, thus, can strongly influence the BEC dynamics. Initially, this dense magnon group decays rapidly due to intense four-magnon scattering processes (see, for example, refs 30,41). This decay closely relates to the jump in the BEC population number shown in Fig. 4. Over the course of time, the density of the parametrically excited magnons decreases, four-magnon scattering decelerates and, eventually, the magnon relaxation attains its intrinsic value, corresponding to the decay rate of the gaseous magnons at the bottom of the magnon spectrum. As is clearly seen in Fig. 4, this nonlinear relaxation behaviour is independent of the laser heating and, thus, cannot be the reason for the temperature-gradient-related BEC dynamics.

We now present a model to describe our experimental findings. The local laser heating process locally changes the saturation magnetization and, thus, induces a weak frequency shift $\delta\omega_c$ between different parts of the magnon condensate. Over the course of time this frequency shift results in an increasing phase gradient in the magnon BEC. As a result, a phase-gradient-induced magnon current or, in other words, a magnon supercurrent, flowing out of the hot region of the focal spot, is excited. This efflux reduces the density of the magnon BEC in the probing point. After some time, the enhanced decrease in the magnon density results in the disappearance of the condensate, and thus in the disappearance of the supercurrent. Consequently, this leads to the recovery of the conventional relaxation dynamics associated with a residual incoherent gaseous magnon phase.

To quantify our interpretation, that a magnon supercurrent is acting, recall that a BEC of magnons can be described by the Gross–Pitaevskii equation for the complex wavefunction $C(\boldsymbol{r},t)=\sqrt{N_c}\exp(i\varphi)$, where $N_c(\boldsymbol{r},t)$ and $\varphi(\boldsymbol{r},t)$ are the magnon number density per unit volume and the BEC phase, respectively. This equation is the well-known equation for the envelope of a narrow wavepacket (see, for example, refs 41,42). It conserves the total number of condensed magnons $\mathcal{N}_c=\int N_c(\boldsymbol{r},t)\,\mathrm{d}\boldsymbol{r}$ and leads to the continuity equation for the BEC density $N_c(\boldsymbol{r},t)$:

$$\frac{\partial N_c}{\partial t}+\sum_i \frac{\partial J_i}{\partial r_i}=0, \quad J_i=\frac{N_c}{2}\sum_j \frac{\partial^2\omega(\boldsymbol{q})}{\partial q_i \partial q_j}\frac{\partial\varphi}{\partial r_j} \tag{1}$$

Here $\boldsymbol{J}(\boldsymbol{r},t)$ is a supercurrent formed by the BEC magnons. In the (x,y)-plane of a YIG film (see Fig. 2d) it has two components

$$J_x=N_c D_x \partial\varphi/\partial x, \quad J_y=N_c D_y \partial\varphi/\partial y \tag{2}$$

where $D_x=\mathrm{d}^2\omega(\boldsymbol{q})/(2\mathrm{d}q_x^2)$ and $D_y=\mathrm{d}^2\omega(\boldsymbol{q})/(2\mathrm{d}q_y^2)$ are the anisotropic dispersion coefficients. A cumbersome analysis of the

magnon spectrum near its bottom[33] shows (see also Methods) that at our experimental conditions $D_x \simeq 21 D_y$ and, thus, $J_x \gg J_y$. This allows us to neglect J_y in the global balance of the magnon numbers and to simplify the problem to a one-dimensional (1D) case along the x-axis (see Fig. 2d).

There are two reasons for the x-dependence of the BEC phase φ in our experiment. The first is the already mentioned temperature dependence of ω_c. Within the hot spot of radius R centred at $x=0$ (that is, for $|x|<R$) the temperature $T(x)$ is higher than the temperature T_0 of the rest of the film (see Fig. 2d). Since in an in-plane magnetized YIG film $\mathrm{d}\omega_c(T)/\mathrm{d}T<0$, the BEC frequency in the spot is smaller than outside: $\delta\omega_c(x)=\omega_c(T(x))-\omega_c(T_0)<0$. Correspondingly, the phase accumulation $\delta\varphi(x)=\delta\omega_c(x)t$ inside of the spot is smaller than in the surrounding cold film. Therefore, the phase gradient $\partial\delta\varphi(x)/\partial x$ is positive for $x>0$ and negative for $x<0$. It means that a thermally induced supercurrent flows out from the spot (mostly in x-direction), as is shown by the red arrows in Fig. 2d:

$$J_T = N_c D_x \frac{\partial(\delta\omega_c t)}{\partial x} \tag{3}$$

This outflow decreases the magnon BEC density $N_c(x)$ in the spot, $|x|<R$, with respect to that in the cold film, where $N_c(x \gg R) = N_c^0$.

Spatial deviations in the density $N_c(x)$ of the magnon condensate constitute the second reason for the variation of its phase $\partial\varphi/\partial x \neq 0$. It results in an additional contribution to the supercurrent, given by equation (1), which can be named a 'dispersive' current J_{dis}. To estimate J_{dis} notice that the 1D Gross–Pitaevskii equation has the self-similar solution $C(x,t)=\mathcal{F}(\xi)$, with $\xi = x^2/(D_x t)$, where the function $\mathcal{F}(\xi)$ satisfies the ordinary differential equation $\xi\,\mathrm{d}\mathcal{F}/\mathrm{d}\xi = i(\mathrm{d}\mathcal{F}/\mathrm{d}\xi + 2\xi\,\mathrm{d}^2\mathcal{F}/\mathrm{d}\xi^2)$. It describes the well known phenomenon of dispersive spreading of a wavepacket with the width $\delta x = \sqrt{D_x t}$ permanently increasing in time. It is worth noticing that exactly the same law is satisfied by the diffusion process with the diffusion current $J_{dif} = D_x(\partial N_c(x)/\partial x)$. Ignoring the difference between the self-similar profiles in the dispersion and the diffusion processes (it is well below the resolution of our experiment), we can estimate the dispersive current J_{dis} by its diffusion counterpart:

$$J_{dis}(x) \simeq -D_x \frac{\partial N_c}{\partial x} \tag{4}$$

This current is directed to the lower $N(x)$ region—that is, towards the hot spot—as shown in Fig. 2d by blue arrows.

A consistent description of the evolution of a parametrically driven magnon system towards BEC may be achieved in the framework of the theory of weak wave turbulence[43], which was further developed in ref. 41 to describe the spin-wave turbulence under parametric excitation. The main tool of this theory is a kinetic equation for the occupation numbers $n(\boldsymbol{q})$ of waves (magnons in our case) presented, for example, in ref. 9. Here we restrict ourselves to the analysis of a crucially simplified version of the kinetic equations—by rate equations for the total number of magnons in particularly chosen parts of the $\boldsymbol{q}$-space shown in Fig. 1. The first part is the BEC with density N_c (orange dot in Fig. 1). The second part is the magnon gas with density N_b at the bottom of the magnon spectrum in close vicinity to the BEC (blue area $\mathbb{R}_b$ surrounding the orange BEC point in Fig. 1). These parts are directly coupled via four-magnon scattering processes ($\mathbb{R}_b \rightarrow$ BEC) and are simultaneously detected due to the finite resolution of the frequency- and wavenumber-resolved BLS set-up. The third part is given by the magnon gas area $\mathbb{R}_g$ above $\mathbb{R}_b$. In our simplified model, which is schematically shown in Fig. 5, the parametrically injected magnons of density N_p (magenta dot in Fig. 1) first populate the gas area $\mathbb{R}_g$ ($N_p \rightarrow \mathbb{R}_g$), and afterwards move to the bottom part $\mathbb{R}_b$ of the magnon spectrum due to four-magnon scattering processes between these areas ($\mathbb{R}_g \rightleftarrows \mathbb{R}_b$).

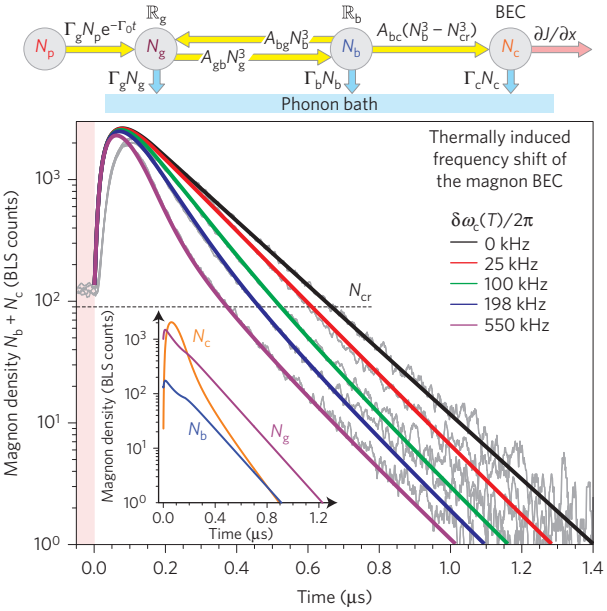

Figure 5 | Theoretically calculated magnon dynamics in a thermal gradient. Theoretical dependencies (coloured lines) of the observable magnon densities ($N_c + N_b$) calculated according to equations (5)–(7) for different temperature-dependent shifts $\delta\omega_c(T)$ of the BEC frequency ω_c are shown in comparison with the corresponding experimental data (grey curves). The upper diagram demonstrates magnon transitions between the q-space parts defined in Fig. 1 (yellow arrows), magnon relaxation (blue arrows) to the phonon bath and a supercurrent outflow (red arrow) from the locally heated magnon BEC described by equations (5)–(7). The inset shows the calculated temporal behaviour of N_c, N_b and N_g for the case of the strongest heating of the magnon BEC.

In the rate equations for the magnon numbers N_g, N_b and N_c we have to account that the kinetic equations for the four-magnon scattering processes conserve the total number of magnons and that the leading term for the magnon flux from the j to the i sub-system is proportional to N_j^3 and, thus, can be written as $A_{ij}N_j^3$, with A_{ij} being dimensional (s^{-1}) phenomenological constants.

Thus, the rate equations take the following form:

$$\frac{\partial N_g}{\partial t} = -\Gamma_g N_g + \Gamma_g N_p e^{-\Gamma_0 t} - A_{gb}N_g^3 + A_{bg}N_b^3 \tag{5}$$

$$\frac{\partial N_b}{\partial t} = -\Gamma_b N_b + A_{gb}N_g^3 - A_{bg}N_b^3 - A_{bc}(N_b^3 - N_{cr}^3)\Theta(N_b - N_{cr}) \tag{6}$$

$$\frac{\partial N_c}{\partial t} = -\Gamma_c N_c + A_{bc}(N_b^3 - N_{cr}^3)\Theta(N_b - N_{cr}) - \frac{\partial J}{\partial x} \tag{7}$$

Here Γ_g, Γ_b and Γ_c are relaxation frequencies of corresponding magnons in the processes that do not conserve magnon numbers (mainly caused by spin–orbit interaction). The second term on the right-hand side of equation (5) represents the external magnon source, and is proportional to the number of parametrically pumped magnons N_p. The factor $\exp(-\Gamma_0 t)$ models the processes of magnon thermalization after the end of the pump pulse. The terms $\propto A_{ij}$ in equations (5)–(7) describe the magnon fluxes between the chosen spectral areas, leading finally to the population of the BEC state. The flux $\mathbb{R}_b \rightarrow$ BEC contains the Heaviside function $\Theta(N_b - N_{cr})$, which involves N_{cr}—a critical number of magnons at which the chemical potential μ of the magnon gas reaches ω_{min}. It is $\Theta(N_b - N_{cr}) = 1$ for $N_b - N_{cr} > 0$ and 0 otherwise. Therefore, for $N_b \leq N_{cr}$ there is no flux of magnons to the condensate. For $N_b > N_{cr}$ this flux appears and an excess of magnons $N_b - N_{cr}$ populates the condensate.

As we have discussed above, the supercurrent J in equation (7) consists of two parts: $J = J_T + J_{dis}$. Their modelling is, probably, the most delicate issue. We adopt the simplest version, assuming a constant temperature gradient from the centre ($x = 0$) of the heated spot to R:

$$J = -B_s N_c \delta\omega_c t + B_{dis}(N_c^0 - N_c) \quad (8)$$

Here, for the coefficients we have $B_s \sim B_{dis} \sim -D_x/R$.

The results of the numerical solution (see Methods) of equations (5)–(8) for different T in the centre of the hot spot and, accordingly, for different $\delta\omega_c(T)$, are shown in Fig. 5 by solid coloured lines together with the respective experimental data. One clearly sees the good agreement between the theoretical and experimental curves. The initial rise of the theoretical curves on the time interval $0 \leqslant t < 0.2\,\mu s$ occurs faster than in the experiment. This is probably due to our simplified model, with only three zones in the $\boldsymbol{q}$-space. We ignore here the multistage character of the $N_p \rightarrow \mathbb{R}_g$ magnon transfer.

In the comparison of our model with experiments performed at different spot temperatures T, we used only one T-dependent parameter $\delta\omega_c(T)$, related to the temperature dependence of the saturation magnetization $M(T)$ of YIG[29]: at standard ambient conditions $dM(T)/dT \simeq -4\ G\ K^{-1}$, giving $d\omega_c/dT = -116\ kHz\,K^{-1}$. For the largest frequency shift ($\delta\omega_c = 550$ kHz), assumed in our calculations, it requires a rather mild heating of the spot by about 4.7 K. This value agrees well with a numerically found temperature rise of 5.7 K in the centre of the focal spot (see Methods).

The occurrence of the supercurrent directly confirms the phase coherency of the observed magnon condensate and fuels expectations of the realization of electrically controlled phase-driven magnon transport[25,26], which can be used in future magnonic devices for low-loss information transfer and processing[44]. Therefore, with this demonstration of a magnon supercurrent in a magnon BEC we have opened the door to studies in the general field of magnonic macroscopic quantum transport phenomena at room temperature as a novel approach in the field of information processing technology.

Methods

Methods, including statements of data availability and any associated accession codes and references, are available in the online version of this paper.

Received 1 March 2016; accepted 22 June 2016; published online 1 August 2016

References

1. Matthews, M. R. *et al*. Vortices in a Bose–Einstein condensate. *Phys. Rev. Lett.* **83,** 2498–2501 (1999).
2. Raman, C. *et al*. Evidence for a critical velocity in a Bose–Einstein condensed gas. *Phys. Rev. Lett.* **83,** 2502–2505 (1999).
3. Bardeen, J., Cooper, L. N. & Schrieffer, J. R. Microscopic theory of superconductivity. *Phys. Rev.* **106,** 162–164 (1957).
4. Page, D., Lattimer, J. M., Prakash, M. & Steiner, A. W. in *Novel Superfluids* Vol. 2 (eds Bennemann, K. H. & Ketterson, J. B.) 505–579 (Oxford Univ. Press, 2014).
5. Borovik-Romanov, A. S., Bun'kov, Yu. M., Dmitriev, V. V. & Mukharskiĭ, Yu. M. Long-lived induction signal in superfluid ^{3}He-B. *JETP Lett.* **40,** 1033–1037 (1984).
6. Butov, L. V. *et al*. Stimulated scattering of indirect excitons in coupled quantum wells: signature of a degenerate Bose-gas of excitons. *Phys. Rev. Lett.* **86,** 5608–5611 (2001).
7. Kasprzak, J. *et al*. Bose–Einstein condensation of exciton polaritons. *Nature* **443,** 409–414 (2006).
8. Balili, R., Hartwell, V., Snoke, D., Pfeiffer, L. & West, K. Bose–Einstein condensation of microcavity polaritons in a trap. *Science* **316,** 1007–1010 (2007).
9. Bunkov, Yu. M. *et al*. High-T_c spin superfluidity in antiferromagnets. *Phys. Rev. Lett.* **108,** 177002 (2012).
10. Amo, A. *et al*. Superfluidity of polaritons in semiconductor microcavities. *Nature Phys.* **5,** 805–810 (2009).
11. Einstein, A. Quantentheorie des einatomigen idealen Gases. *Sitz.ber. Preuss. Akad. Wiss. Phys.* **22,** 261–267 (1924).
12. Einstein, A. Quantentheorie des einatomigen idealen Gases – Zweite Abhandlung. *Sitz.ber. Preuss. Akad. Wiss. Phys.* **23,** 3–14 (1925).
13. Anderson, M. H., Ensher, J. R., Matthews, M. R., Wieman, C. E. & Cornell, E. A. Observation of Bose–Einstein condensation in a dilute atomic vapor. *Science* **269,** 198–201 (1995).
14. Davis, K. B. *et al*. Bose–Einstein condensation in a gas of sodium atoms. *Phys. Rev. Lett.* **75,** 3969–3973 (1995).
15. Borovik-Romanov, A. S., Bun'kov, Yu. M., Dmitriev, V. V. & Mukharskiĭ, Yu. M. Observation of phase slippage during the flow of a superfluid spin current in ^{3}He-B. *JETP Lett.* **45,** 124–128 (1987).
16. Borovik-Romanov, A. S. *et al*. Observation of a spin-current analog of the Josephson effect. *JETP Lett.* **47,** 478–482 (1988).
17. Bunkov, Yu. M. & Volovik, G. E. Spin vortex in magnon BEC of superfluid ^{3}He-B. *Physica C* **468,** 609–612 (2008).
18. Bunkov, Yu. M. Spin superfluidity and coherent spin precession (Fritz London Memorial Prize Lecture). *J. Phys. Condens. Matter* **21,** 164201 (2009).
19. Fröhlich, H. Bose condensation of strongly excited longitudinal electric modes. *Phys. Lett. A* **26,** 402–403 (1968).
20. Klaers, J., Schmitt, J., Vewinger, F. & Weitz, M. Bose–Einstein condensation of photons in an optical microcavity. *Nature* **468,** 545–548 (2010).
21. Rodriguez, S. R. K., Feist, J., Verschuuren, M. A., Garcia Vidal, F. J. & Gómez Rivas, J. Thermalization and cooling of plasmon-exciton polaritons: towards quantum condensation. *Phys. Rev. Lett.* **111,** 166802 (2013).
22. Kalafati, Yu. D. & Safonov, V. L. Thermodynamic approach in the theory of paramagnetic resonance of magnons. *Sov. Phys. JETP* **68,** 1162–1167 (1989).
23. Demokritov, S. O. *et al*. Bose–Einstein condensation of quasi-equilibrium magnons at room temperature under pumping. *Nature* **443,** 430–433 (2006).
24. Troncoso, R. E. & Núñez, Á. S. Josephson effects in a Bose–Einstein condensate of magnons. *Ann. Phys.* **346,** 182–194 (2014).
25. Nakata, K., van Hoogdalem, K. A., Simon, P. & Loss, D. Josephson and persistent spin currents in Bose–Einstein condensates of magnons. *Phys. Rev. B* **90,** 144419 (2014).
26. Nakata, K., Simon, P. & Loss, D. Magnon transport through microwave pumping. *Phys. Rev. B* **92,** 014422 (2015).
27. Büttner, O. *et al*. Linear and nonlinear diffraction of dipolar spin waves in yttrium iron garnet films observed by space- and time-resolved Brillouin light scattering. *Phys. Rev. B* **61,** 11576–11587 (2000).
28. Sandweg, C. W. *et al*. Wide-range wavevector selectivity of magnon gases in Brillouin light scattering spectroscopy. *Rev. Sci. Instrum.* **81,** 073902 (2010).
29. Cherepanov, V., Kolokolov, I. & L'vov, V. The saga of YIG: spectra, thermodynamics, interaction and relaxation of magnons in a complex magnet. *Phys. Rep.* **229,** 81–144 (1993).
30. Serga, A. A. *et al*. Bose–Einstein condensation in an ultra-hot gas of pumped magnons. *Nature Commun.* **5,** 3452 (2014).
31. Gurevich, A. G. & Melkov, G. A. *Magnetization Oscillations and Waves* (CRC Press, 1996).
32. Kreisel, A., Sauli, F., Bartosch, L. & Kopietz, P. Microscopic spin-wave theory for yttrium-iron garnet films. *Eur. Phys. J. B* **71,** 59–68 (2009).
33. Kalinikos, B. A., Kostylev, M. P., Kozhus, N. V. & Slavin, A. N. The dipole-exchange spin wave spectrum for anisotropic ferromagnetic films with mixed exchange boundary conditions. *J. Phys. Condens. Matter* **2,** 9861–9877 (1990).
34. Serga, A. A. *et al*. Brillouin light scattering spectroscopy of parametrically excited dipole-exchange magnons. *Phys. Rev. B* **86,** 134403 (2012).
35. Neumann, T., Serga, A. A., Vasyuchka, V. I. & Hillebrands, B. Field-induced transition from parallel to perpendicular parametric pumping for a microstrip transducer. *Appl. Phys. Lett.* **94,** 192502 (2009).
36. Clausen, P. *et al*. Stimulated thermalization of a parametrically driven magnon gas as a prerequisite for Bose–Einstein magnon condensation. *Phys. Rev. B* **91,** 220402(R) (2015).
37. Bozhko, D. A. *et al*. Formation of Bose–Einstein magnon condensate via dipolar and exchange thermalization channels. *Low Temp. Phys.* **41,** 1024–1029 (2015).
38. Nowik-Boltyk, P., Dzyapko, O., Demidov, V. E., Berloff, N. G. & Demokritov, S. O. Spatially non-uniform ground state and quantized vortices in a two-component Bose–Einstein condensate of magnons. *Sci. Rep.* **2,** 482 (2012).
39. Autti, S. *et al*. Self-trapping of magnon Bose–Einstein condensates in the ground state and on excited levels: from harmonic to box confinement. *Phys. Rev. Lett.* **108,** 145303 (2012).
40. Li, F., Saslow, W. M. & Pokrovsky, V. L. Phase diagram for magnon condensate in yttrium iron garnet film. *Sci. Rep.* **3,** 1372 (2013).

41. L'vov, V. S. *Wave Turbulence Under Parametric Excitations* (*Applications to Magnetics*) (Springer, 1994).
42. Landau, L. D. & Lifshitz, E. M. *Quantum Mechanics* (*Non-Relativistic Theory*), *Course of Theoretical Physics* Vol. 3 (Pergamon Press, 1977).
43. Zakharov, V. E., L'vov, V. S. & Falkovich, G. *Kolmogorov Spectra of Turbulence* (*Wave Turbulence*) (Springer, 1992).
44. Chumak, A. V., Vasyuchka, V. I., Serga, A. A. & Hillebrands, B. Magnon spintronics. *Nature Phys.* **11,** 453–461 (2015).

Acknowledgements

Financial support from the Deutsche Forschungsgemeinschaft (project INST 161/544-3 within the Transregional Collaborative Research Centre SFB/TR 49 'Condensed Matter Systems with Variable Many-Body Interactions' and project VA 735/1-2 within the priority programme SPP 1538 'Spin Caloric Transport'), from EU-FET (Grant InSpin 612759) and from the State Fund for Fundamental Research of Ukraine (SFFR) is gratefully acknowledged. D.A.B. is supported by a fellowship of the Graduate School Material Sciences in Mainz (MAINZ) through DFG funding of the Excellence Initiative (GSC-266). We are also indebted to Y. Tserkovnyak, S. Eggert, A. N. Slavin, V. S. Tiberkevich, K. Nakata, D. Loss and V. L. Pokrovsky for fruitful discussions. We also acknowledge I. I. Syvorotka (Scientific Research Company 'Carat', Lviv, Ukraine) for supplying us with the YIG film sample.

Author contributions

A.A.S. and B.H. contributed to the experimental idea, planned and supervised the project. D.A.B., P.C., V.I.V. and A.A.S. carried out the experiments. D.A.B. and P.C. contributed to the experimental set-up. D.A.B. carried out the numerical analysis. G.A.M., A.P. and V.S.L. developed the theoretical model. F.H. performed temperature simulations. All authors analysed the experimental data and discussed the results.

Additional information

Reprints and permissions information is available online at www.nature.com/reprints. Correspondence and requests for materials should be addressed to B.H.

Competing financial interests

The authors declare no competing financial interests.

Methods

Sample. The yttrium iron garnet (YIG, $Y_3Fe_5O_{12}$) sample is 5 mm long and 1 mm wide. The single-crystal YIG film of 5.6 μm thickness has been grown in the (111) crystallographic plane on a gadolinium gallium garnet (GGG, $Gd_3Ga_5O_{12}$) substrate by liquid-phase epitaxy.

Time- and wavevector-resolved Brillouin light scattering spectroscopy. The magnon dynamics was analysed by means of time- and wavevector-resolved BLS spectroscopy[27,28] in the back-scattering geometry.

Brillouin light scattering can be interpreted as the diffraction of the probing light from a moving Bragg grating produced by a magnon mode. As a result, some portion of the scattered light is shifted in frequency by the frequency of this mode. In addition, the diffraction from the grating leads to a transfer of momentum during this process. For example, the in-plane component of the wavevector $\boldsymbol{q}_L$ of the incident light is inverted by a magnon mode propagating along the projection of a probing beam on a thin magnetic film if the magnon wavenumber q satisfies the Bragg condition $q=-2q_L\sin(\Theta)$, where Θ is the angle of incidence. By changing the angle Θ, wavevector selection of in-plane magnons with wavevector $\boldsymbol{q}$ can be implemented. In our experiment, the probing beam of 532 nm wavelength generated by a single-mode solid-state laser is focused by a precise objective onto a microstrip resonator placed just below the YIG film. In this case, the inelastically scattered light with the inverted in-plane wavevector component $-\boldsymbol{q}_L\sin(\Theta)$ is reflected back to the objective and collected for further analysis. Both the sample and the magnetic system are mounted on a rotating stage to allow the variation of the angles $\Theta=\Theta_{q\|}$ (the angle lies in the plane containing the bias magnetic field $\boldsymbol{H}$) and $\Theta=\Theta_{q\perp}$ (the angle lies in the plane perpendicular to $\boldsymbol{H}$), holding the magnetization conditions constant. By varying these angles, magnons with wavevectors parallel and perpendicular to the magnetic field $\boldsymbol{H}$ are resolved[28]. The described set-up allowed us to resolve wavevector values up to $1.5\times10^5\,\mathrm{rad\,cm^{-1}}$. For the particular experiment the wavevector resolution was $2\times10^3\,\mathrm{rad\,cm^{-1}}$.

The light collected by the objective is directed to a multipass tandem Fabry–Pérot interferometer[45–47] for frequency selection. At the output of the interferometer, a single-photon-counting avalanche diode detector is placed. The output of the detector is connected to a fast data acquisition module, which enables accumulation and further analysis of the envelope of the temporal dynamics of the scattered photons. The time resolution is based on a stroboscopic technique—the experiment is repeated many times (the repetition rate of the experiment was 1 ms) with the same parameters. When the pumping pulse is applied, it triggers the internal counter in the acquisition module, which has an internal clock rate of 1 ns, defining the temporal resolution of the experimental set-up[27]. Every time the detector registers a photon, this event is recorded to a database which collects the number of arrived photons at each clock cycle. The frequency of the interferometer's transmission is also recorded, thus providing frequency information for each detected photon.

Determination of anisotropic dispersion coefficients. The dispersion coefficients $D_x=\mathrm{d}^2\omega(\boldsymbol{q})/(2\,\mathrm{d}q_x^2)$ and $D_y=\mathrm{d}^2\omega(\boldsymbol{q})/(2\,\mathrm{d}q_y^2)$ were found by a numerical calculation of the dispersion curvature near the global minimum of the magnon spectrum. The detailed procedure of the dispersion calculation can be found in ref. 33. For our experimental conditions the obtained values are $D_x=7.45\,\mathrm{cm^2\,s^{-1}}$ and $D_y=0.355\,\mathrm{cm^2\,s^{-1}}$. Thus, $D_x\simeq21D_y$.

Fitting model parameters. The numerical values of the parameters used in equations (5)–(7) are presented in Table 1.

The relaxation frequencies Γ_g, Γ_b and Γ_c are taken from the measurements of the relaxation rate of a freely evolving BEC in the no-heating case (see the black curve in Fig. 4) and the relaxation rate of gaseous magnons (the magnon-gas-related curves in Fig. 4) as well. Due to the relatively small spectral distance between the magnons participating in the condensation process, their relaxation frequencies are practically identical and, for simplicity, are replaced by the same mean value $\Gamma=6.1$ MHz.

In a numerical solution of our model we have chosen the initial BEC value $N_c^0=0$, because it is known that the gaseous magnons do not populate the lowest energy state in the case of pumping at higher power levels[30]. As a result, no magnon condensation occurs during the pump action, and the BEC in the global energy minimum (ω_{min},q_{min}) is formed after the termination of the pump pulse. In such a case the initial value N_b^0 (in units of BLS counts) can be taken from our experimentally measured value N_b+N_c at $t=0$ (in Fig. 5). The critical density N_{cr} is approximately determined as the magnon number, where the transition from the BEC-dominated to the magnon-gas-dominated relaxation behaviour occurs (see Figs 4 and 5). The magnon numbers N_p and N_g^0, as well as the scattering efficiencies A_{ij}, are responsible for the intensity of magnons scattering to the bottom of the spectrum. Therefore, their values can be found from the simultaneous iterative fitting of the two most different curves (black and purple curves in Fig. 5), taking into account the initial increase in N_b+N_c at $t\leqslant0.1\,\mu$s. All mentioned parameters are independent of temperature, and thus they have been chosen to be the same in all plots. Finally, all fittings in Fig. 5 were obtained by only adjusting $\delta\omega_c$ in the supercurrent term equation (8).

Table 1 | Temperature independent parameters of rate equations.

Parameter	Value	Units	Physical meaning
$\Gamma_g,\Gamma_b,\Gamma_c$	6.1×10^6	s^{-1}	Magnon damping to the lattice
Γ_0	2.63×10^7	s^{-1}	Magnon gas thermalization rate
N_c^0	0	-	Initial number of condensed magnons
N_b^0	135	-	Initial number of bottom magnons
N_g^0	1,000	-	Initial number of gaseous magnons
N_p	18,500	-	Initial number of thermalized magnons
A_{gb}	43	s^{-1}	Scattering efficiency of gaseous magnons to bottom magnon states ($\mathbb{R}_g\rightarrow\mathbb{R}_b$)
A_{bg},A_{bc}	14,250	s^{-1}	Scattering efficiency of bottom magnons to gaseous ($\mathbb{R}_b\rightarrow\mathbb{R}_g$) and to condensed ($\mathbb{R}_b\rightarrow$ BEC) magnon states
N_{cr}	85	-	A critical number of magnons at which the chemical potential μ of the magnon gas reaches ω_{min}

Table 2 | Material parameters for COMSOL simulation.

Material	Density ρ $\mathrm{kg\,m^{-3}}$	Thermal conductivity k $\mathrm{W\,m^{-1}\,K^{-1}}$	Heat capacity C_P $\mathrm{J\,kg^{-1}\,K^{-1}}$
YIG[50]	5,170	6	570
GGG[50]	7,080	8	400
AlN[51]	3,260	175	738
Cu[52]	8,700	400	385
Air[52]	1.205	0.0257	1,005

Simulation of the laser heating. The numerically found value of the temperature increase of 5.7 K in the centre of the laser focal spot was determined by solving a 3D heat-transfer model of the experimental set-up using the COMSOL Multiphysics software[48] equipped with the Heat Transfer Module[49]. Hereby, the conventional heat conduction differential equation is solved taking into consideration the boundary conditions applied to the model, the material parameters of the materials used (see Table 2) and the applied heat source.

The model comprises a 0.5-mm-thick GGG substrate with a YIG film of 5.6 μm thickness, a 17-μm-thick and 50-μm-wide Cu microstrip placed on a 0.64-mm-thick AlN substrate, and ambient air conditions outside. The extent of the entire model is $2\times2\,\mathrm{mm^2}$ in plane and around 1.16 mm out of plane. The temperature at all edges of the model is kept fixed to 293.15 K to simulate the stable boundary condition far away from the heated area. The laser heating is modelled by a cylindrical heat source placed into the YIG layer above the centre of the microstrip antenna. Heat is deposited exponentially along the film thickness and has a Gaussian distribution in the film plane reflecting the shape of the laser focal spot. The experimentally determined 67% absorption of green light of 532 nm wavelength in the 5.6-μm-thick YIG layer (GGG is practically transparent for this light) results in a total heat power of 6.3 mW.

Data availability. The data that support the plots within this paper and other findings of this study are available from the corresponding author upon reasonable request.

References

45. Lindsay, S. M., Anderson, M. W. & Sandercock, J. R. Construction and alignment of a high performance multipass vernier tandem Fabry-Pérot interferometer. *Rev. Sci. Instrum.* **52,** 1478–1486 (1981).
46. Mock, R., Hillebrands, B. & Sandercock, R. Construction and performance of a Brillouin scattering set-up using a triple-pass tandem Fabry-Pérot interferometer. *J. Phys. E* **20,** 656–659 (1987).

47. Hillebrands, B. Progress in multipass tandem Fabry-Perot interferometry: I. A fully automated, easy to use, self-aligning spectrometer with increased stability and flexibility. *Rev. Sci. Instrum.* **70,** 1589–1598 (1999).
48. COMSOL Multiphysics. *The Platform for Physics-based Modeling and Simulation* https://www.comsol.com/comsol-multiphysics
49. Heat transfer module. *Software for General-purpose Modeling of Heat Transfer in Solids and Fluids* https://www.comsol.com/heat-transfer-module
50. Schreier, M. *et al*. Magnon, phonon, and electron temperature profiles and the spin Seebeck effect in magnetic insulator/normal metal hybrid structures. *Phys. Rev. B* **88,** 094410 (2013).
51. Haynes, W. M., Lide, D. R. & Bruno, T. J. *Handbook of Chemistry and Physics* (CRC Press, 2005).
52. COMSOL material library. https://www.comsol.com/material-library